



# The variation law and mechanism of titanium alloy MIG welding process under the synergistic effect of coaxial dual channel gas path

Chuanchuan Jia<sup>1,2</sup> · Guorui Sun<sup>2</sup> · Boqiao Ren<sup>2</sup> · Jiuqing Liu<sup>1</sup> · Chao Chen<sup>2</sup>

Received: 26 April 2024 / Accepted: 5 August 2024  
© International Institute of Welding 2024

## Abstract

MIG welding still had a lot of potential in the titanium alloy industry with many advantages. How to achieve stable process and forming was still a hard nut to crack for titanium alloy MIG welding. The conventional MIG welding torch had a small coverage of shielding gas which causes an obvious insufficient capability of isolating air. Therefore, this study introduced the fluid field composite MIG process, proposed a novel strategy of titanium alloy MIG welding process under the synergistic effect of coaxial dual channel gas path, and had explored the impact of the synergistic effect of internal gas flow( $Q$ ) and external gas flow( $q$ ) on the welding process from three aspects: droplet transfer characteristics and weld surface morphology, weld cross-section. The results showed that the form of “one large droplet + several small droplets” was always maintained during transition process.  $Q$  mainly impacted on the variation law of the droplet transition; however, the length of transition period was mainly affected by  $q$ . In addition, the arc length was reduced meanwhile the geometric parameters of welds' cross-section had more regular changes after adding  $q$ . The surface morphology was the worst when  $Q$  acted solely; however, it was straight and uniform after adding  $q$ . When  $q=40\text{L/min}$  and  $Q=15\text{L/min}$ , the coverage and protective effect of shielding gas was excellent, no turbulence was generated, and no pores generated in the cross-section of the weld. It was easier to obtain a more stable forming of titanium alloy MIG welding when  $Q$  and  $q$  worked together.

**Keywords** MIG composite welding · Dual channel gas path · Droplet transfer · Welding forming · Titanium alloy

## 1 Introduction

Welding was a process of metal fusing and joining that melts metals rapidly and then cools speedily to form a sturdy welded joint [1]. The common welding processes included gas metal arc welding (GMAW), shielded metal arc welding (SMAW), friction welding (FW), laser welding (LW), tungsten inert gas welding (TIG), activated tungsten inert

gas welding (A-TIG), etc. [2] Metal inert gas arc welding (MIG) was a type of GMAW, which has great development prospects as a common welding process for metal additive manufacturing [3].

MIG welding has been extensively utilized in aerospace, transportation, and other fields, possessing numerous commendable traits such as high metal deposition efficiency, simple operation, and high material utilization [4–7]. However, the drawbacks such as excessive spatter, high heat input, low surface quality of welds, and poor microstructure and properties of welded joints were attached to conventional MIG welding typically, which limits the development of MIG welding [8]. At present, the composite MIG processes, such as ultrasonic-MIG composite welding and laser-MIG composite welding, have been developed to address the aforementioned defects and improve welding efficiency by researchers [9–12]. Lin Shen et al. [13], for instance, used laser MIG composite welding technology to weld 7B05-T5 aluminum alloy plates and analyzed the stress corrosion behavior of the welded joints, explaining the propagation mechanism of stress corrosion cracks in the welded joints.

---

Recommended for publication by Commission XII - Arc Welding Processes and Production Systems

✉ Jiuqing Liu  
nefujdljq@163.com

✉ Chao Chen  
chaochenaw@126.com

<sup>1</sup> College of Mechanical and Electrical Engineering, Northeast Forestry University, Harbin 150040, China

<sup>2</sup> Key Laboratory of Automobile Materials, School of Materials Science and Engineering, Jilin University, Changchun 130025, China

Liu et al. [14] used alternating magnetic field to assist laser MIG composite welding, improving the penetration depth of 316 stainless steel welding joints and achieving good welding results. Yuji et al. [15] used plasma MIG composite welding to weld aluminum alloy A5052. The experiment confirmed that plasma welding and MIG welding can form a seamless integrated metal melt pool, and quantitatively measured the part of flow field in the melt pool.

Ti and titanium alloys have been applied to many fields of biomedical, aerospace, and marine engineering extensively, which attributes to its many superiorities, high strength, low density, excellent corrosion resistance, and strong resistance to plastic deformation, for example [16–20]. In addition, if there was not a good enough shielding atmosphere during the welding process, the alloys were prone to embrittlement, oxidation, and nitriding owing to its strong high-temperature activity, which causes a weakening of weld quality [21–23]. Therefore, shielding titanium alloys from the air was an essential aspect that could not be ignored in MIG welding process. Different titanium alloy welding processes were also rapidly evolving with the speedy development of related industries. Researchers continuously developed innovative titanium alloy composite welding processes, for instance, laser-MIG composite welding, to reduce production costs and improve welding stability and quality, increase production efficiency [16, 24–26]. Unfortunately, MIG was not used as the main process for titanium alloy welding on account of the inferiorities of poor arc stability, excessive splashing, small shielding gas coverage and poor shielding effect; instead, relatively stable welding processes such as TIG welding and laser welding were preferred to employ, which has severely limited the application of MIG

in the field of titanium alloy welding [27]. Therefore, it was urgent to broaden the scope of Ti-alloy welding processes and develop Ti-alloy-fit MIG welding processes with strong process stability and excellent shielding atmosphere.

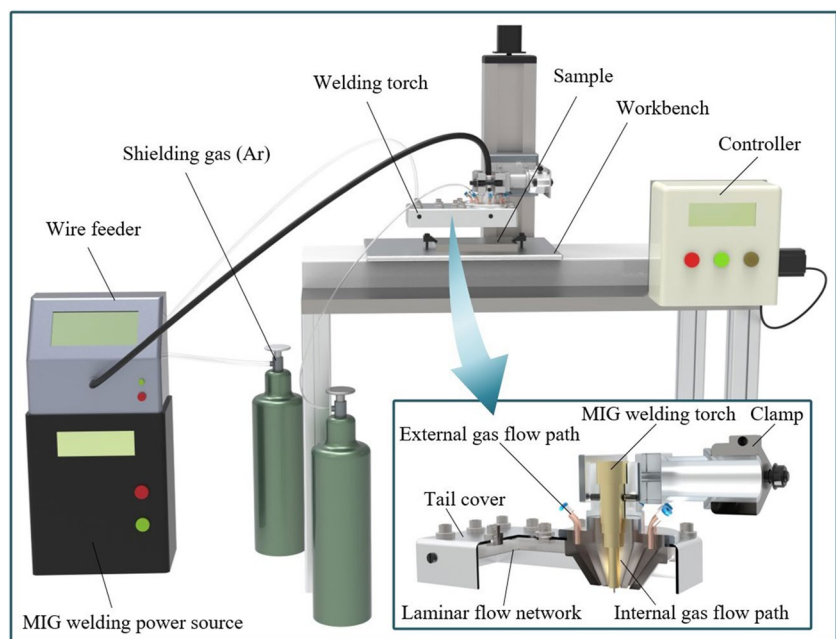
To develop a novel Ti-alloy MIG welding process, this study proposed a new strategy of Ti-alloy MIG welding process under the synergistic effect of coaxial dual channel gas paths. It was noteworthy that current researchers were primarily engaged in the Ti-alloy MIG composite welding adding energy field and heat sources, neglecting the fluid field conducted by shielding gas. Consequently, this technique not only addressed the limited range of shielding gas in traditional MIG but also introduced a dual-channel gas flow fluid field composite MIG welding process. We designed a welding torch independently for the new composite process and conducted experiments using the variable-controlling approach to study the synergistic effect of the internal gas flow rate ( $Q$ ) and the external gas flow rate ( $q$ ) on the MIG welding process.

## 2 Experimental process

### 2.1 Materials

The experimental platform of new MIG welding process is shown in Fig. 1. The experimental system for new MIG welding process included a wire feeder (FastMig WFX300-T), a MIG power source (FastMig X350), a welding torch, a linear guide rail controller, samples, and a workbench. The welding torch used in the experiment was developed independently. In this study, the Ti-6Al-4 V (TC4) titanium alloy welding

**Fig. 1** Schematic diagram of the experimental platform for new MIG welding process



wire with a diameter of 1.2 mm and the TC4 titanium alloy plates with the dimension of 100 mm×20 mm×8 mm were employed as welding materials. The elemental composition of TC4 titanium alloy is shown in Table 1. The oxide layer and oil stains on the surface of the base material could affect welding quality seriously and cause welding defects. Therefore, before the experiment, an angle grinder was used to polish the surface of the base material to remove the oxide layer, and acetone was used to clean the surface of the base material to remove oil stains. The MIG welding power source was selected as the direct current MIG mode. The transition mode was selected as the droplet transfer to facilitate the observation of the droplet transfer process. The basic process parameters are shown in Table 2.

## 2.2 Experimental methods

Three sets of experiments were set up to study the effects of internal gas flow rate ( $Q$ ) and external gas flow rate ( $q$ ) on the MIG welding process, namely the control group and experimental group I and experimental group II, respectively. The control group studied the effect of changes in single factor internal gas flow rate on the stability of the welding process, i.e., the conventional MIG welding; here the external gas flow rate was 0, and the internal gas flow rate was changed by equal span, which is in three groups: 10L/min, 15L/min, 20L/min. Experimental group I studied the effect of single factor external gas flow rate on the stability of the welding process. At this time, the internal gas flow rate was 0, and the external gas flow rate was changed by an equal span, in order of five groups: 10L/min, 20L/min, 30L/min, 40L/min, 50L/min. Experimental group II studied the effect of the combination of internal and external gas flow rates on the welding process. At this time, the fixed external gas flow rate was 40L/min, and the internal gas flow rate was changed with equal span, which were sequentially divided into four groups: 5L/min and 10L/min, 15L/min, 20L/min.

Argon gas (Ar) was employed as the welding shielding gas. A high-speed camera was used for capture of the welding process, with a frame rate set to 2000 fps, which means the time interval between taking two photos was 0.5 ms. When observing the cross-section of the weld seam, metallographic samples were prepared using a wire cutting machine and were polished until there were no obvious scratches. Then, the metallographic surface was corroded with a corrosion solution (a solution of 5% HF, 10% HNO<sub>3</sub> and rest water by volume), and finally the cross-sectional morphology of the weld seam was captured by a stereomicroscope.

**Table 1** The composition of TC4 alloy

Element	Al	V	Fe	O	Si	C	N	H	Else	Ti
Content	5.5–6.8	3.5–4.5	0.3	0.2	0.15	0.1	0.05	0.01	0.5	Rest

**Table 2** Welding process parameters

Wire feeding speed	Welding voltage	Welding speed
8 m/min	30 V	5 mm/s

## 3 Results

### 3.1 Droplet transfer

The control group studied the effect of changes in single factor internal gas flow rate ( $Q$ ) on the stability of the welding process. At this time, the external gas flow rate ( $q$ ) was 0, and the internal gas flow rate was changed at an equal span, in order of 10 L/min and 15 L/min, and 20 L/min.

During the stable transition phase, we selected a transition cycle precisely as a representative of the entire process; the images of droplet transfer are shown in Fig. 2. It found that in the new device, the droplet transfer process exhibited a regular transfer pattern of “one larger droplet + several smaller droplets” in one cycle under the ordinary MIG process (with an external gas flow rate of 0). The transition period of large droplets was longer, while the transition period of small droplets was shorter. During the welding process, short-circuit transition was prone to occur during the transition of large droplets, while the transition of small droplets always maintained a typical droplet transition. After statistical analysis, it was found that within 5 s, there was one large droplet short-circuit transition at  $Q=10$ L/min (as shown in Fig. 2a), three large droplet short-circuits transitions at  $Q=15$ L/min (as shown in Fig. 2b), and nine large droplet short-circuits transitions at  $Q=20$ L/min (as shown in Fig. 2c). When a short-circuit occurred, the current had an upsurge while the voltage instantly decreased to 0, and then returned to normal, as shown in the schematic diagram of current–voltage waveform (Fig. 3d). According to Fig. 3, the transition period of large droplets decreased first and then increased with the raising of internal gas flow rate, while the transition period of small droplets increased first and then decreased with the increase of internal gas flow rate. At  $Q=15$  L/min, the transition period for large droplets was the shortest, about 118 ms, and the transition period for small droplets was the longest, about 22.5 ms. As  $Q$  increased, the overall size of large droplets increased. When  $Q=20$ L/min, the maximum size of large droplets was 3.3 mm, but the size of small droplets remained basically unchanged.

Within a transition period, the arc with the maximum length and energy concentration was selected as the

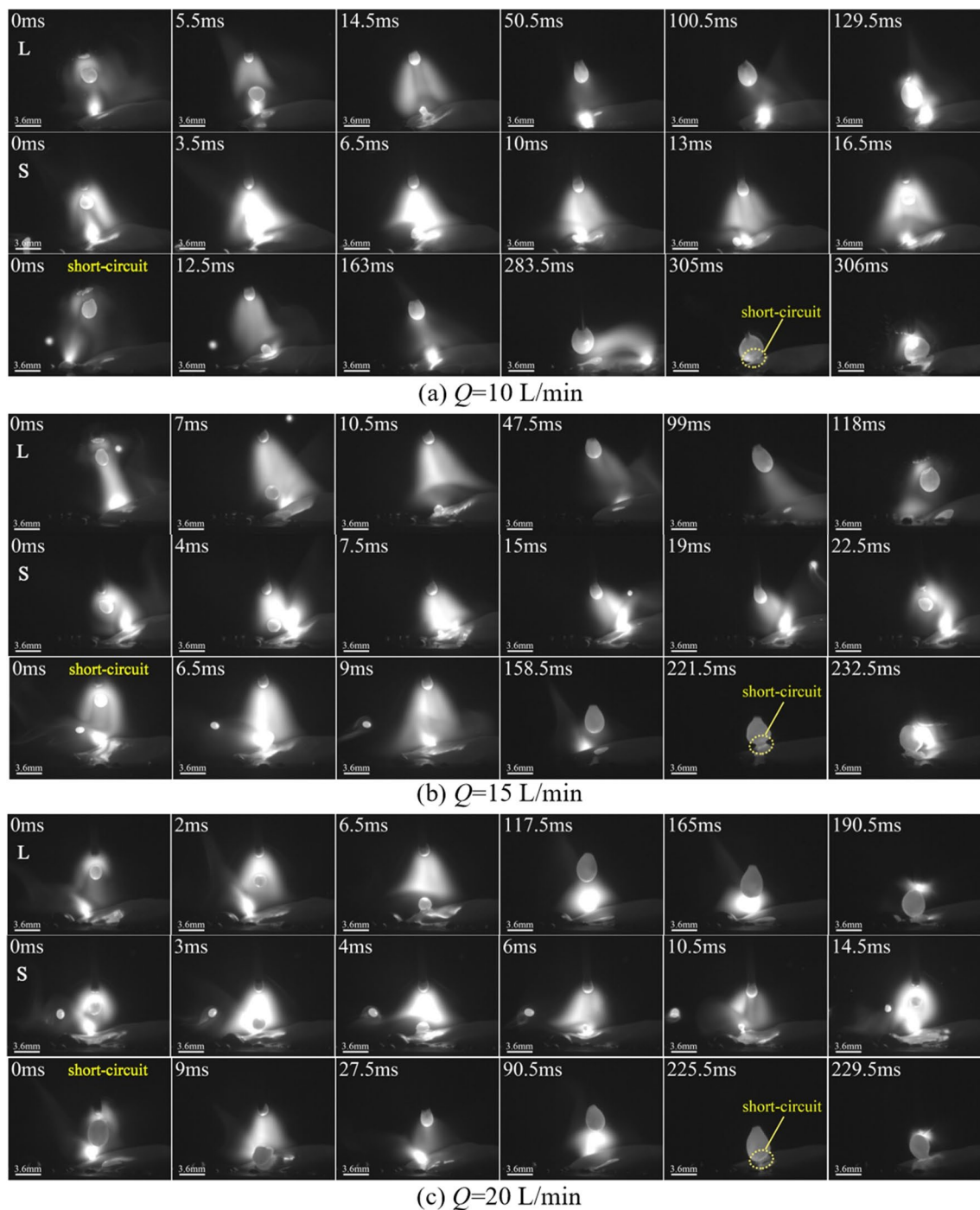
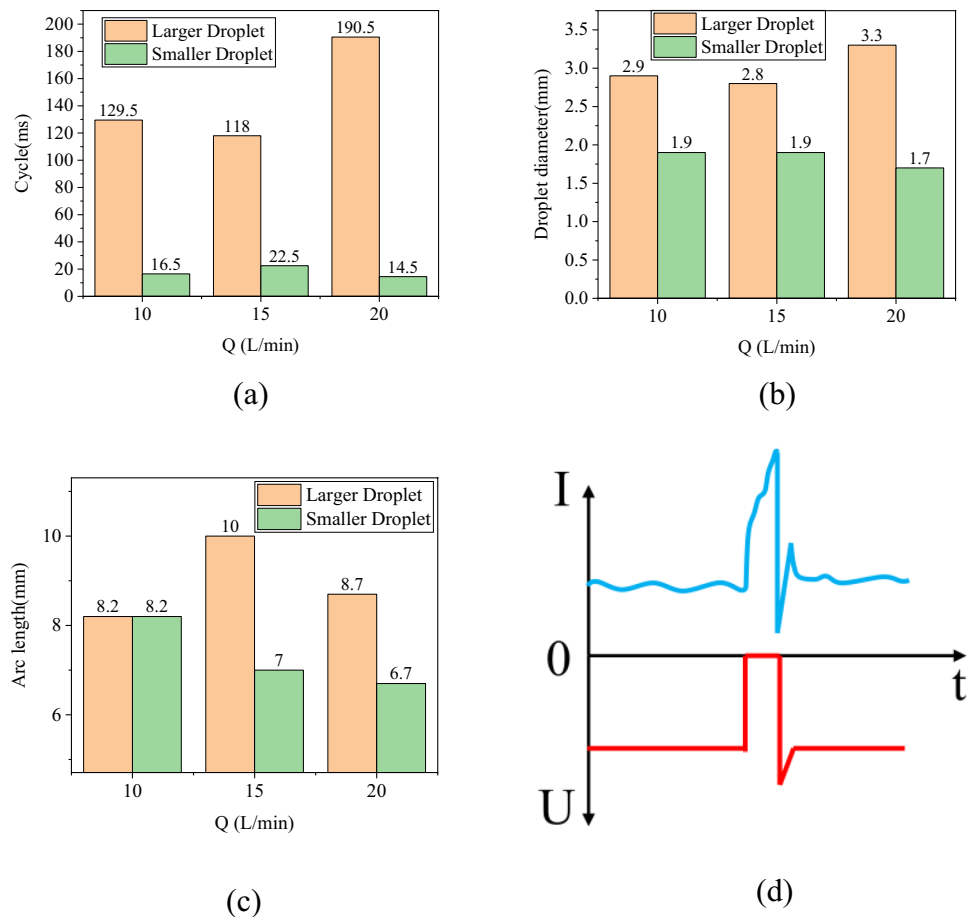


**Fig. 2** Images of droplet transfer with different welding conditions ( $q=0$ )

representative of the arc for this transition period. PS software was utilized to measure the distance between the bottom of the wire and the molten pool, which is the arc length. The measurement of MIG arc length under different internal gas flow rates is shown in Fig. 3c. As  $Q$  increased, the arc length during the transition of large droplets reached its maximum at  $Q=15$  L/min, which is

10 mm, but it decreased slightly at  $Q=20$  L/min. Therefore, there was no significant linear relationship between the arc length and  $Q$  during the transition of large droplets. The arc length during the transition of small droplets decreased with the growth of  $Q$ . The maximum arc length was 8.2 mm when  $Q=10$  L/min, and the minimum arc length was 6.7 mm when  $Q=20$  L/min.

**Fig. 3** Characteristic parameters of droplet transfer with different welding conditions ( $q=0$ ) and schematic diagram of current–voltage waveform. **a** Transfer cycle. **b** Droplet diameter. **c** Arc length. **d** Schematic diagram of current–voltage waveform



Experimental group I studied the effect of single factor external gas flow rate ( $q$ ) on the stability of the welding process. At this time, the internal gas flow rate ( $Q$ ) was 0. Changing the external gas flow rate resulted in five groups: 10L/min and 20L/min, 30L/min, 40L/min, 50L/min. The images of droplet transfer are shown in Fig. 4. Analysis showed that the addition of external gas flow did not change the transition form of “one larger droplet + several smaller droplets” mentioned above, and the transition period of larger droplets was still longer, while that of smaller droplets was shorter. The transition period of large droplets showed an overall increasing trend with the growth of external gas flow rate. At  $q=10$  L/min, the transition period of large droplets was the smallest, which is 141.5 ms. At  $q=40$  L/min, the transition period of large droplets fluctuated with a smaller value of 144 ms. The transition period of small droplets decreased first and then increased with the raising of external gas flow rate. The minimum was 17 ms when  $q=20$  L/min, and the maximum was 26 ms when  $q=40$  L/min. However, compared with the control group, the change in droplet transition period in this group was not significant, and the maximum value was lower than that in the control group. As  $q$  increased, the size of small droplets remained largely unaffected, while the size of large droplets

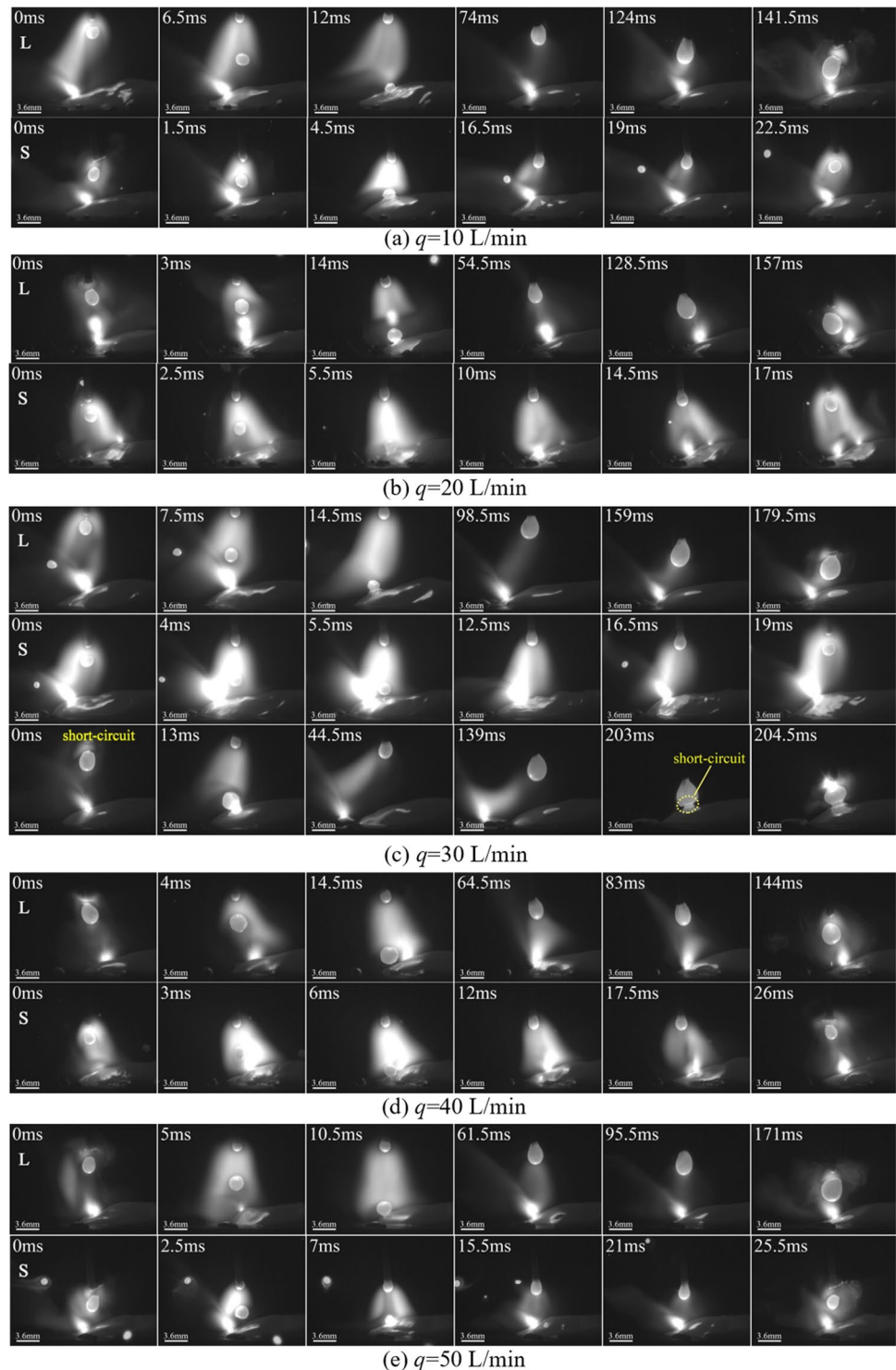
underwent slight changes. The maximum size of large droplets was 3.3 mm, and the maximum size of small droplets was 2.1 mm, both obtained at  $q=30$  L/min. And according to statistics, only one large droplet short-circuit transition occurred within 5 s when  $q=30$  L/min, as shown in Fig. 4c.

The length of MIG arc was measured under different external gas flow rates in experimental group I, and the results are shown in Fig. 5c. During the transition of large droplets, the arc length became unstable with the increase of  $q$ . When  $q=10$  L/min, the arc length was maximum at 12.5 mm, and when  $q=20$  L/min, the arc length was minimum at 10.1 mm. During the transition of small droplets, as  $q$  increased, the arc length first increased and then reduced. When  $q=30$  L/min, the arc length was maximum at 9.4 mm, and when  $q=50$  L/min, the arc length was minimum at 7 mm. By observing the transition photos of the droplets, it was found that compared to the control group, the arc shape in this group was more chaotic, the arc direction was unstable, and the arc length was generally higher than that in the control group.

Experimental group II studied the effect of the combination of internal and external gas flow rates on the welding process. At this time, the external gas flow rate ( $q$ ) was fixed at 40L/min, and the internal gas flow rate ( $Q$ )

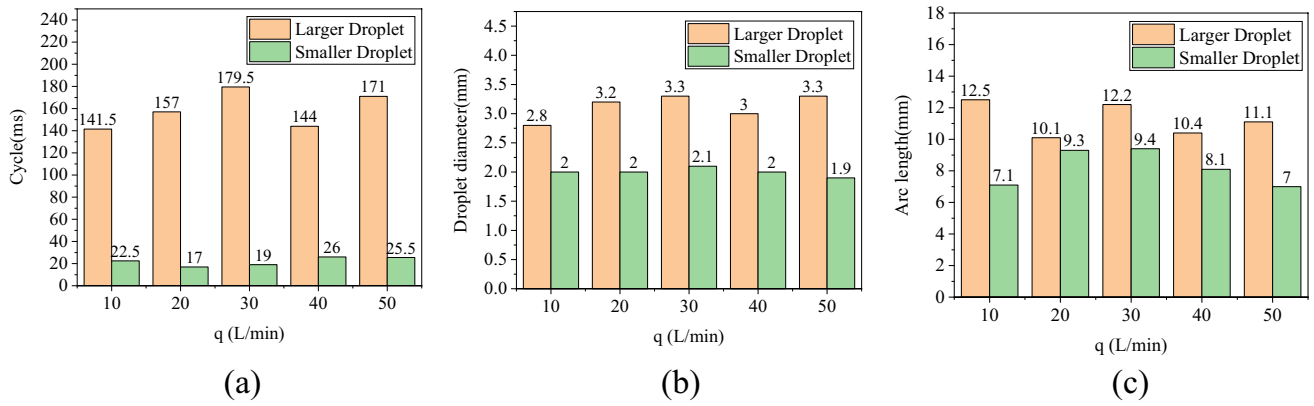


**Fig. 4** Images of droplet transfer with different welding conditions ( $Q=0$ )



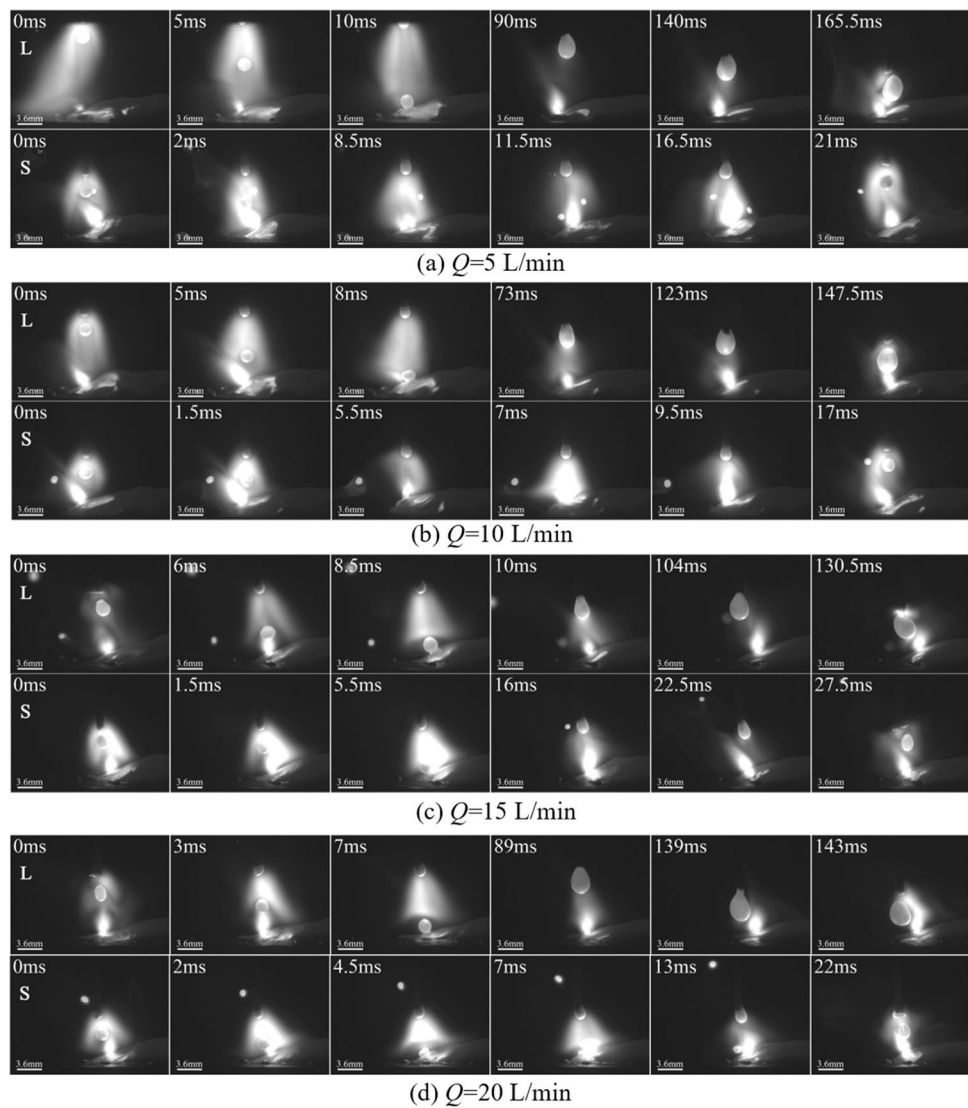
was changed, followed by four groups: 5L/min and 10L/min, 15L/min, 20L/min. The photos of droplet transition are shown in Fig. 6. Through comparative analysis, it was found that when adding internal gas flow based on an external gas flow rate of  $q = 40$  L/min, the transition form of “one larger droplet + several smaller droplets” found in the control group was still maintained, and the rule of

“longer transition period for larger droplets and shorter transition period for smaller droplets” was not affected. According to statistics, no short-circuit transfer occurred within 5 s. As the internal gas flow rate increased, the transition period of large droplets first decreased and then increased, while the transition period of small droplets fluctuated up and down in a small range. When  $Q = 15$  L/



**Fig. 5** Characteristic parameters of droplet transfer with different welding conditions ( $Q=0$ ). **a** Transfer cycle. **b** Droplet diameter. **c** Arc length

**Fig. 6** Images of droplet transfer with different welding conditions ( $q=40$  L/min)



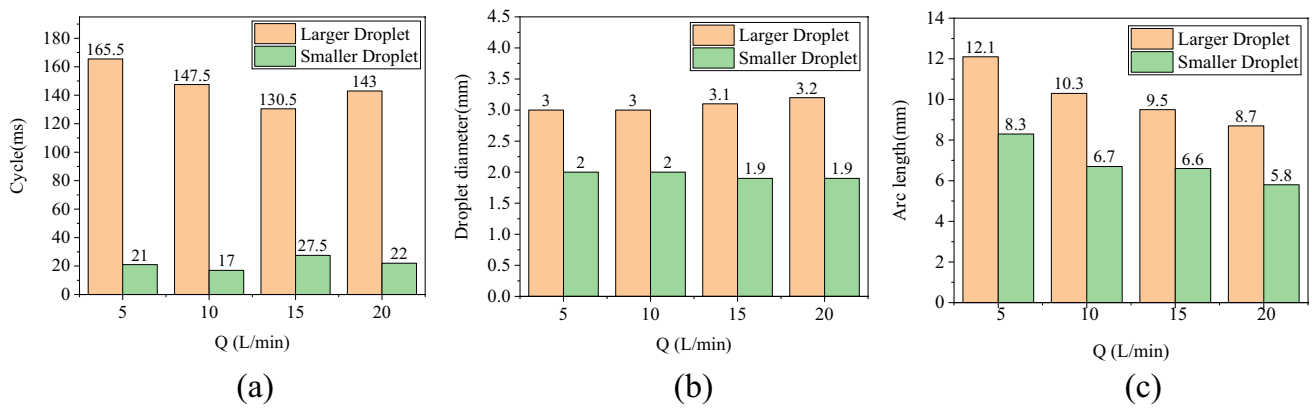


**Fig. 7** Characteristic parameters of droplet transfer with different welding conditions ( $q=40$  L/min). **a** Transfer cycle. **b** Droplet diameter. **c** Arc length

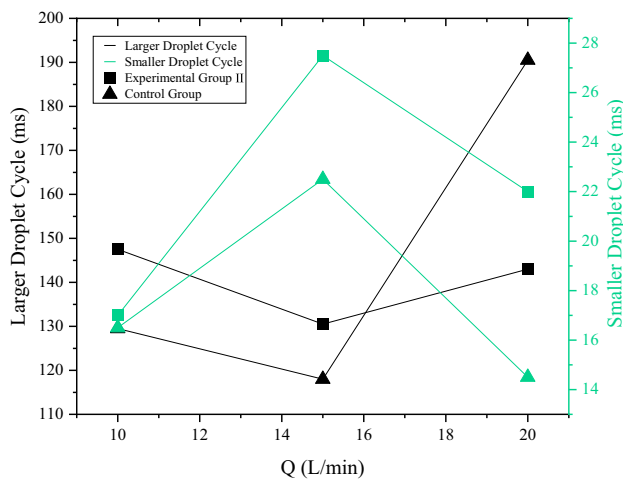


**Fig. 8** Droplet transfer cycle with different welding conditions for different group

min, the minimum transition period of large droplets was 130.5 ms, and when  $Q=10$  L/min, that of small droplets was 17 ms.

Compared with the control group, it was found that when  $Q=20$  L/min, the addition of external gas flow  $q=40$  L/min reduced the transition period of large droplets, but still increased the transition period of small droplets. Moreover, at  $Q=10$  L/min and 15 L/min, there was an increasing trend in the transition periods of both large and small droplets compared with the control group. Excluding accidental factors, it was found that at the same  $Q$  value, the addition of external gas flow would increase the transition period of both large and small droplets to a certain extent. However, the addition of  $q$  did not affect the variation pattern of the two, as shown in Fig. 8. According to Fig. 7b, it could be observed that the synergistic effect of the internal gas flow and the external gas flow had little effect on the droplet size.

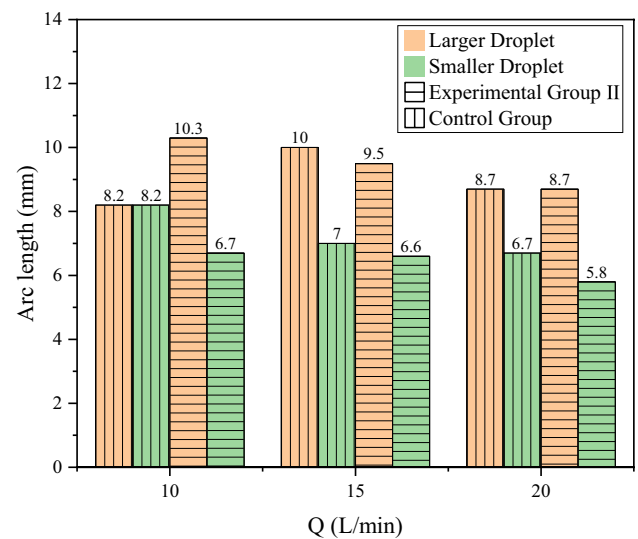


**Fig. 9** Arc length with different welding conditions for different group

The length of MIG arc was measured under different internal gas flow rates in experimental group II, and the results are shown in Fig. 7c. At  $q=40$  L/min, as  $Q$  increased, the arc length of both large and small droplet transitions decreased steadily (Fig. 8). When  $Q=5$  L/min, the maximum arc length was 12.1 mm and 8.3 mm, respectively. When  $Q=20$  L/min, both were the smallest, 8.7 mm and 5.8 mm respectively. Compared with the control group, it was found that under the action of  $Q$ , the addition of  $q$  slightly reduced the arc length, as shown in Fig. 9.

### 3.2 Surface morphology of weld seam

The surface morphology of the weld seam in the control group is shown in Fig. 10. The overall surface morphology



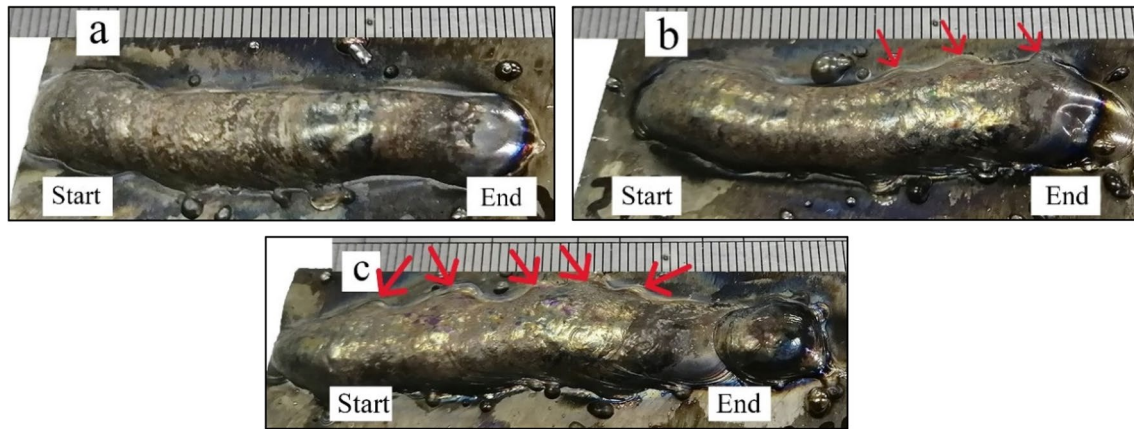


**Fig. 10** Surface morphology of welds under different welding parameters ( $q=0$ ). **a**  $Q=10$  L/min. **b**  $Q=15$  L/min. **c**  $Q=20$  L/min

of the control group welds was poor. As  $Q$  increased, there were more and more weld nodules (as indicated by the red arrow in the Fig. 10), which made the welds increasingly uneven. All welds exhibited bending, and the surface morphology of the welds was the worst when  $Q=20$  L/min. In the above welding process, the droplet was subjected to the combined force exerted by the arc and  $Q$  on it before falling into the molten pool, as well as the upward surface tension and the downward gravity of the droplet itself. In the experiment, it was found that the arc formed between the welding wire and the molten pool rotated irregularly around the surface of the droplet, while the horizontal component of the combined force exerted by the arc and  $Q$  on the droplet did not reach equilibrium at this time. Consequently, there would be a horizontal offset during the droplets fell into the molten pool, which causes the molten pool to also shift, resulting in a curved morphology of the weld seam. And the MIG arc was unstable, which is manifested in the occurrence of arc extinction during

arc initiation and termination, resulting in discontinuous welds.

The surface morphology of the weld seam in experimental group I is shown in Fig. 11. In this group, the surface morphology was relatively uniform, and there was no significant change in width. Surprisingly, the problem of weld seam bending was improved, which indicates that the external gas flow could effectively improve the trouble of horizontal force imbalance during the process of droplet falling. And compared with the control group, there were almost no weld nodules in the welds of this group, and the sides of the welds were relatively neat, indicating that the welding process was relatively stable and there was almost no short-circuit transition. When  $q=40$  L/min, there was a narrowing phenomenon of the weld seam at the arc stopping position, which is caused by the instability of the MIG arc.

The surface morphology of the weld seam in experimental group II is shown in Fig. 12. The weld seam was relatively uniform with no significant changes in width,

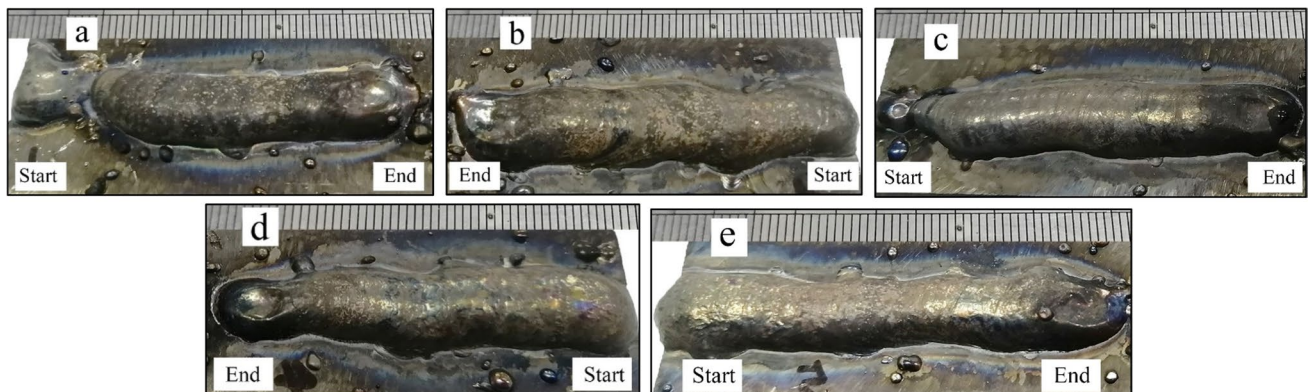


**Fig. 11** Surface morphology of welds under different welding parameters ( $Q=0$ ). **a**  $q=10$  L/min. **b**  $q=20$  L/min. **c**  $q=30$  L/min. **d**  $q=40$  L/min. **e**  $q=50$  L/min

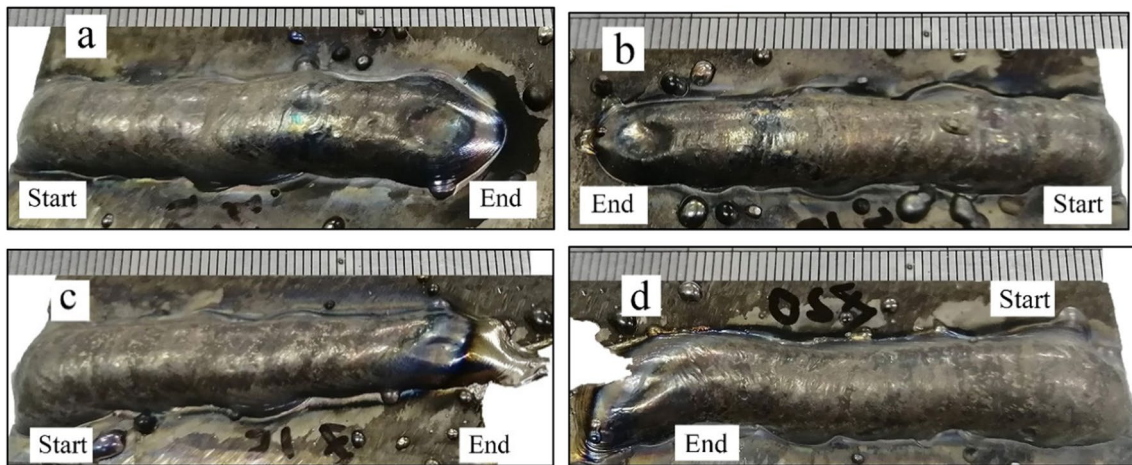


**Fig. 12** Surface morphology of welds under different welding parameters ( $q=40$  L/min). **a**  $Q=5$  L/min. **b**  $Q=10$  L/min. **c**  $Q=15$  L/min. **d**  $Q=20$  L/min

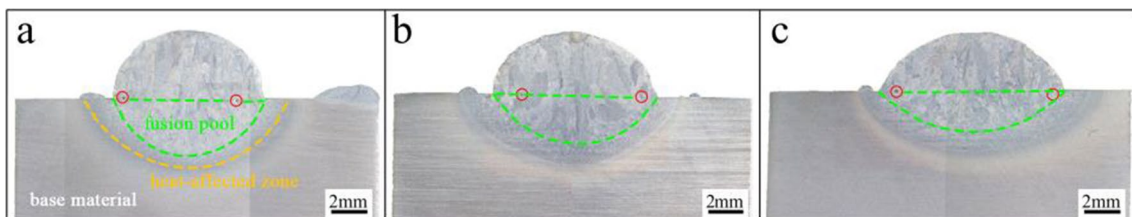


**Fig. 13** Weld cross-section under different welding parameters ( $q=0$ ). **a**  $Q=10$  L/min. **b**  $Q=15$  L/min. **c**  $Q=20$  L/min

and the spreading state of the weld seam was almost consistent with the previous two sets of experiments. Compared with the control group, there was no significant bending in the weld morphology of this group, which confirms the conclusion drawn in experiment group I that the addition of external gas flow could effectively reform the issue of horizontal force imbalance while the droplets fell and verifies that the addition of external gas flow could obtain better weld surface morphology.

The images revealed that all weld surfaces were oxidized, lacking a silver-white metallic luster. This was due to the fact that titanium alloys required a protective atmosphere not only during welding but also post-welding until the temperature decreased. A laminar flow net was installed within the tail cover, ensuring a uniform flow of shielding gas within the tail hood, which prevents negative pressure caused by excessive gas flow by which air was potentially sucked in the hood and compromised the protective atmosphere. The observed oxidation in the experiment was due to the workpiece's brief stay in the tail cover after welding: it came into contact with air before the temperature had a chance to drop, leading to oxidation—not due to any flawed design in the tail cover structure.

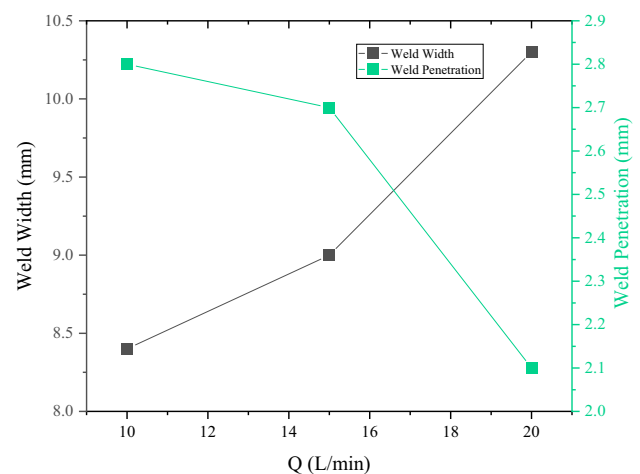


**Fig. 14** Geometric parameters of weld cross-section under different welding parameters ( $q=0$ )

### 3.3 Cross-section of weld seam

The cross-section of the weld seam in the control group is shown in Fig. 13, and the geometric parameters of it are provided in Fig. 14. Through analysis, an increasing trend

could be observed in weld width with the growth of internal gas flow rate ( $Q$ ). At  $Q=20\text{L/min}$ , the weld width reached its maximum, about 10.3 mm, with a change rate of about 22.6% compared to  $Q=10\text{L/min}$ . In terms of weld penetration, the weld penetration decreased obviously continuously as  $Q$  growing. At  $Q=10\text{L/min}$ , the maximum penetration depth was about 2.8 mm, and then decreased continuously. At  $Q=20\text{L/min}$ , the minimum penetration depth was about 2.1 mm, with a change rate of 25%. Within the allowable range of measurement error, it could be inferred that the changes in internal shielding gas flow rate ( $Q$ ) had a slightly stronger impact on the weld penetration than on the weld width under conventional MIG. There were a handful of visible small pores in the cross-section of the weld seam, and these pores were mostly located near the edge of the melt pool, as indicated by the red circle mark.

The cross-section of the weld seam in experimental group I is shown in Fig. 15, and Fig. 16 provides the geometric parameters of the weld seam cross-section. It could be familiarized that the weld width first increased and then decreased with the growth of external gas flow rate ( $q$ ) when  $Q$  was 0. When  $q=20\text{L/min}$ , the weld width was maximum, about 9.5 mm, and the change rate was about 20.3% compared to  $q=10\text{L/min}$ . Within the range of  $q=20\sim 50\text{L/min}$ , the weld width was greater than that at  $q=10\text{L/min}$ . It could be also seen that as  $q$  increased, the fusion width of the weld seam tended to increase. When  $q=40\text{L/min}$ , although the melt width slightly grew, there was still a decreasing trend compared to the melt width of  $q=20\text{L/min}$ , and it was close to the melt width of  $q=50\text{L/min}$ , with a change rate of about 3.8% compared to  $q=10\text{L/min}$ . In terms of weld penetration, the overall penetration depth of the weld seam tended to decrease as  $q$  raised. The maximum melting depth was about 2.9 mm when  $q=10\text{L/min}$ , and then it decreased to the minimum melting depth when  $q=50\text{L/min}$ , which is about 2.2 mm, with a change rate of about 24.1%. Within the

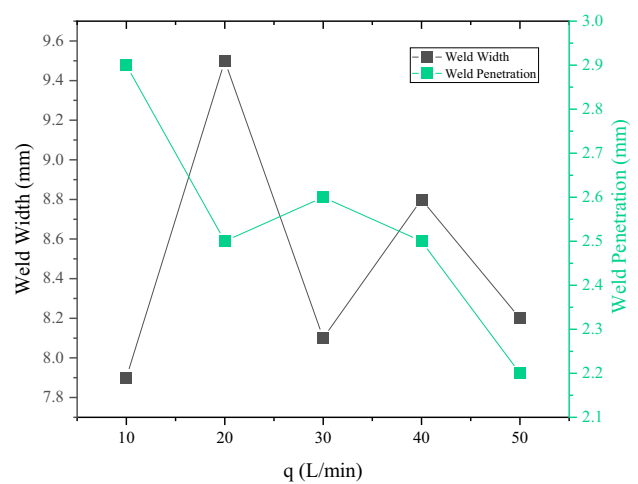


Fig. 16 Geometric parameters of weld cross-section under different welding parameters ( $Q=0$ )

allowable range of measurement error, it could be inferred that the changes in external gas flow rate had also a slightly stronger influence upon the weld penetration than on the weld width.

The cross-section of the weld seam showed that a large single hole appeared at  $q=10\text{L/min}$ , and the holes decreased with the growth of  $q$ . No holes appeared at  $q=40\text{L/min}$ , but small pores appeared again at  $q=50\text{L/min}$ . Pores of all were also mostly located near the edge of the melt pool.

The cross-section of the weld seam in experimental group II is shown in Fig. 17, and the geometric parameters of the weld seam cross-section are provided in Fig. 18. It was obviously that the weld width first decreased and then increased as the internal gas flow rate ( $Q$ ) increased, when the external flow rate was  $q=40\text{L/min}$ . The weld width was about 10.1 mm while  $Q=5\text{L/min}$ , and when  $Q=15\text{L/min}$ , the weld width was the smallest, about 8.0 mm, with

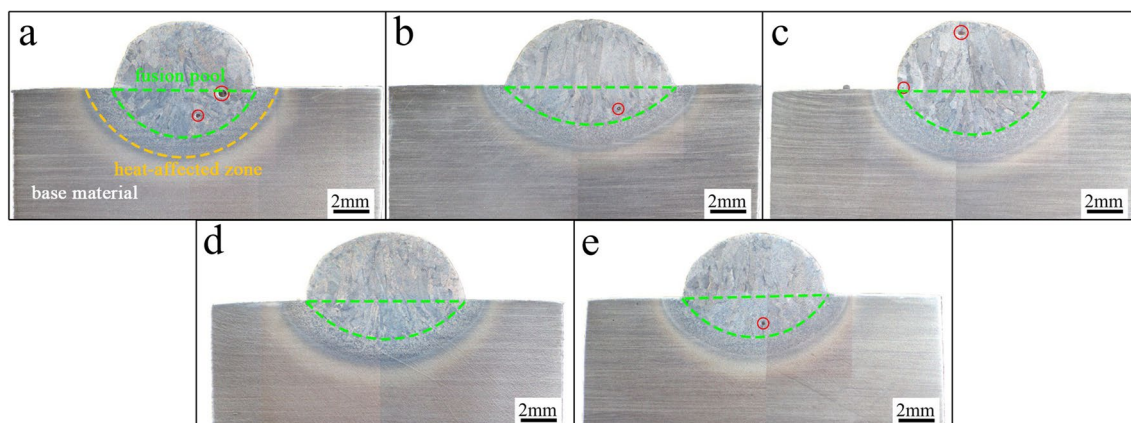
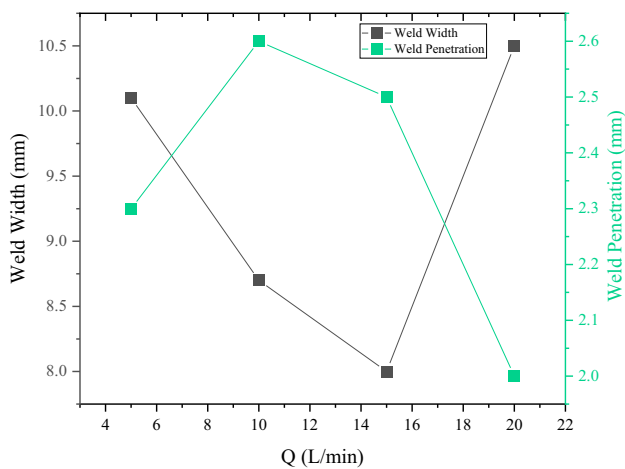
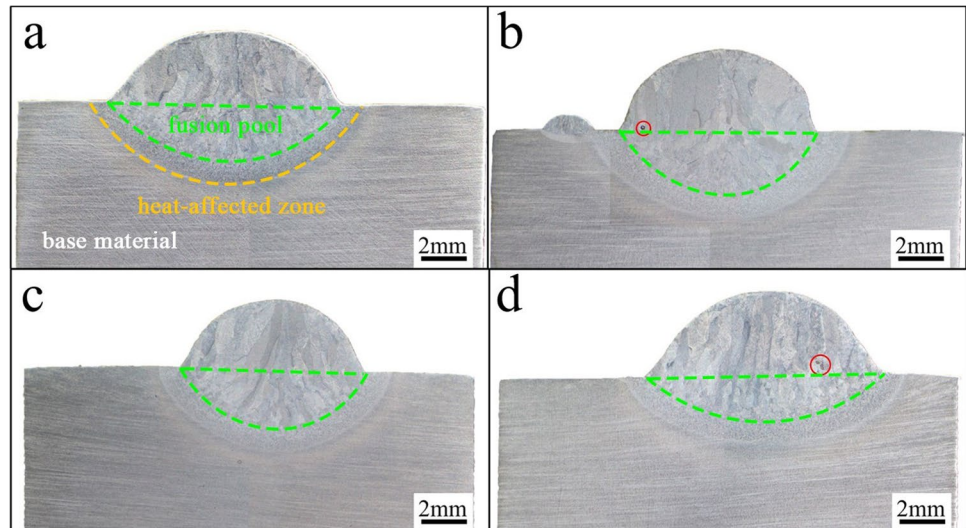


Fig. 15 Weld cross-section under different welding parameters ( $Q=0$ ). a  $q=10\text{ L/min}$ . b  $q=20\text{ L/min}$ . c  $q=30\text{ L/min}$ . d  $q=40\text{ L/min}$ . e  $q=50\text{ L/min}$



**Fig. 17** Weld cross-section under different welding parameters ( $q=40$  L/min). **a**  $Q=5$  L/min. **b**  $Q=10$  L/min. **c**  $Q=15$  L/min. **d**  $Q=20$  L/min



**Fig. 18** Geometric parameters of weld cross-section under different welding parameters ( $q=40$  L/min)

a change rate of about 20.8%. The weld width was the largest when  $Q=20$  L/min, which is about 10.5 mm, with a change rate of about 31.3%. In terms of weld penetration, when the external gas flow rate was  $q=40$  L/min, the weld penetration first increased and then decreased as the growth of the internal gas flow rate. When  $Q=10$  L/min, the maximum weld penetration was about 2.6 mm, with a change rate of about 13.0% compared to  $Q=5$  L/min. Compared with the control group, the variation character of weld penetration and width was not changed basically by the addition of external gas flow rate under the same parameters. However, the values of weld penetration depth and width slightly decreased after adding  $q$ , as shown in Fig. 19. At  $Q=10$  L/min and 20 L/min, a single visible small pore emerged in the weld cross-section near the edge of the melt pool.

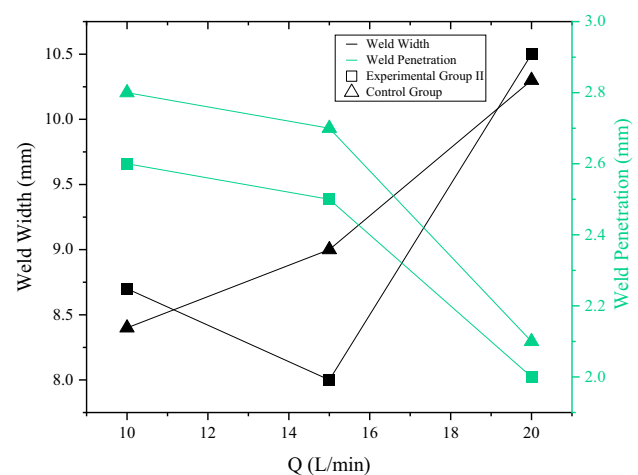


**Fig. 19** Geometric parameters of weld cross-section with different welding conditions for different group

## 4 Discussion

### 4.1 Droplet transfer and weld surface morphology

In the control group of the internal gas flow ( $Q$ ) acting alone, as  $Q$  increased, the transition period of large droplets sharply increased to 190.5 ms at  $Q=20$  L/min, with a change rate of 47% compared to  $Q=10$  L/min. The droplet size and arc length also increased during the transition of large droplets. The images of the droplet transfer exposed that most of the transition process was occupied by the transition of large droplets, and with the increase of  $Q$ , a short-circuit transition appeared in the large droplets, but the transition of small droplets always maintained a typical droplet transition. Generally, short-circuit transition

is a transition mode in which, in the case of a short arc, a short-circuit occurs in contact with the molten pool during the process of droplets growth, and then the arc extinguishes, the droplets transfer to the molten pool under the action of electromagnetic force (necking effect) and surface tension [28]. Obviously, the short-circuit transition phenomenon that occurred in the control group did not follow this pattern. The mechanism of the short-circuit transition phenomenon when the internal gas flow acted alone was as follows.

During the process of falling, droplets were subjected to gravity, plasma flow force, surface tension, and electromagnetic force [29, 30]. In the vertical direction, it was mainly subjected to the combined force of downward gravity  $F_g$ , upward surface tension  $F_\gamma$ , the longitudinal component  $F_m$  of electromagnetic force, and the longitudinal component  $F_d$  of plasma flow force, which can be expressed using Formulas (1) to (4) [31–34]. Due to the influence of arc shape, there were two situations where the electromagnetic force hindered or promoted the transition of droplets in the vertical direction, and the component force, while in the horizontal direction, was manifested as necking effect at the connection between the droplets and the wire on the one hand, and on the other hand, compressing the droplets to contact with the molten pool, forming a liquid bridge.

$$F_g = \frac{4}{3}\pi r_d^3 \rho g \tag{1}$$

$$F_\gamma = 2r_w \pi \gamma \tag{2}$$

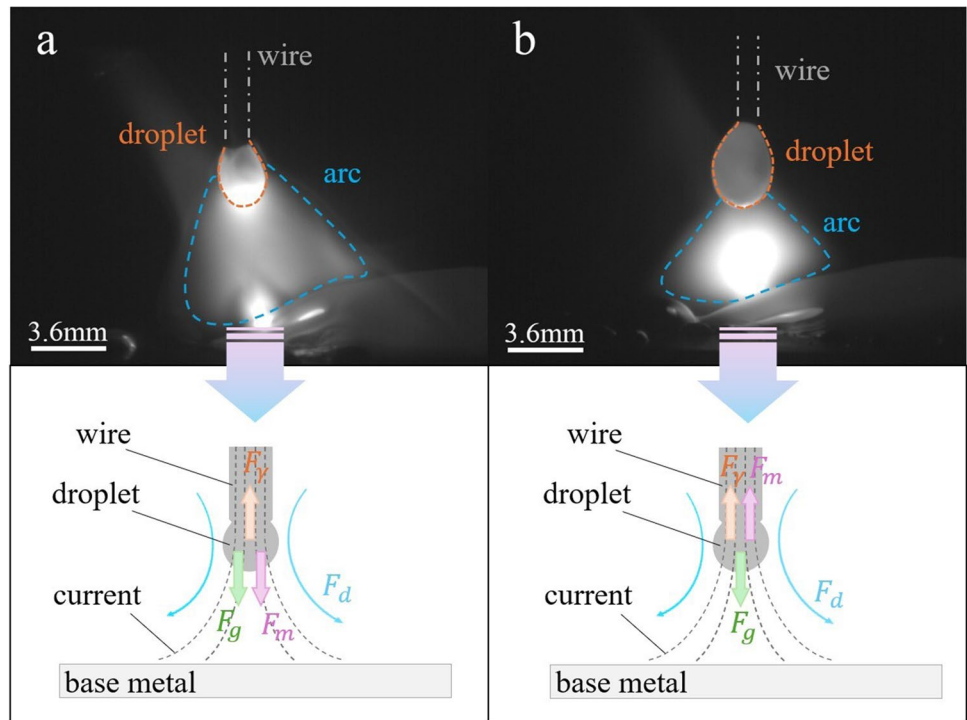
$$F_m = \frac{\mu_0 I^2}{4\pi} \left[ \ln \frac{r_d \sin \theta}{r_w} - \frac{1}{4} - \frac{1}{1 - \cos \theta} + \frac{2}{(1 - \cos \theta)^2} \ln \frac{2}{1 + \cos \theta} \right] \tag{3}$$

$$F_d = C_d A_p \left( \frac{\rho_f v_f^2}{2} \right) \tag{4}$$

where  $r_d$  is the droplet radius,  $\rho$  is the density of liquid metal,  $g$  is the gravitational acceleration,  $r_w$  is the radius of the welding wire,  $\gamma$  is the surface tension coefficient,  $I$  is the welding current,  $\mu_0$  is the vacuum magnetic permeability,  $\theta$  is the half cone angle of the arc,  $C_d$  is the drag coefficient,  $A_p$  is the area of action of the plasma gas flow,  $\rho_f$  is the protective gas density, and  $v_f$  is the gas flow velocity.

When  $Q = 10\text{L/min}$ , the force acting on the large droplets is shown in Fig. 20a. The arc position was in the upper middle part of the droplets in this moment, and the electromagnetic force promoted the transition of the droplets, leading a shorter transition period; frequency of the short-circuit transition for the droplets was also diminished accordingly. As  $Q$  increased to  $20\text{L/min}$ , the force acting on the droplets is shown in Fig. 20b. The arc could not cover the droplets at this time, causing a hinderance of the electromagnetic force to the transition, which makes the transition of large droplets difficult, resulting in an increasing transition period; therefore, there was enough time for them to grow fully (the

**Fig. 20** Schematic diagram of the force acting on a large droplet: **a**  $Q = 10\text{L/min}$ ; **b**  $Q = 20\text{L/min}$





transition period reached 190.5 ms when  $Q=20\text{L/min}$ ). The arc space was exceeded gradually as the size of the large droplets continued to increase, followed by direct contact of the droplets with the molten pool, leading to the occurrence of short-circuit transition. And with the growth of  $Q$ , the obstruction of electromagnetic force caused a continuously increasing transition period (Fig. 3a), and then, the size of large droplets also became larger and larger (Fig. 3b); therefore, the frequency of short-circuit transition increased naturally. Within the same time (5 s), nine short-circuit transitions occurred at  $Q=20\text{L/min}$ .

The force on the droplets in the horizontal direction was unbalanced, causing a deviation in this direction when it grew and fell, which leads to the bending of the weld seam in turn. The welding process became increasingly unstable with the growth of  $Q$ . The surface morphology of the weld seam also accounted for the instability. There were more and more weld nodules as  $Q$  increased. When  $Q=20\text{L/min}$ , there were the most weld nodules, and the surface morphology of the weld seam was the worst.

In the experimental group I of the external gas flow ( $q$ ) acting alone, only at  $q=30\text{ L/min}$ , a short-circuit transition merely occurred once within 5 s. According to Fig. 5, both the transition period and the size of the large droplets reached their maximum value. However, the arc length did not increase significantly, so the large droplets grew fully, leading to short-circuit transitions. Surprisingly, no short-circuit transition occurred under other external gas flow parameters, illustrating that the external gas flow had an effectively suppression to short-circuit transition. After elaborating the area of action of the plasma gas flow  $A_p$  in formula (4), the plasma flow force  $F_d$  can be expressed as formula (5).

$$F_d = 0.5C_d\rho_f v_f^2 \pi r_d^2 \left(1 - \frac{r_w^2}{2r_d^2}\right) \quad (5)$$

By analyzing Figs. 3 and 5, it could be confirmed that the droplets' radius  $r_d$  generally increased when  $q$  acting alone compared to the control group. According to formula (5), the plasma flow force acting on the droplets also increased with the growth of droplets' radius, which promotes the transition of the droplets. According to Fig. 4, it was found that even though the arc morphology was unstable and irregular, it could cover the droplets basically. Therefore, the electromagnetic force  $F_m$  also promoted the transition of the droplets (analogous to Fig. 20a) at this time. Whilst the arc length was also increased generally compared to the control group, therefore, after the droplets grew, it detached smoothly from the welding wire and entered into the molten pool under the combined force, and no short-circuit transition occurred. There was no short-circuit transition during the experimental process with  $q$  acting alone, so the surface morphology of

the weld seam was better compared with the control group, with almost no weld nodules and higher quality of forming. The external gas flow could improve the imbalance of the horizontal component of the resultant force mentioned in the control group during the falling process of droplets, which contributes to the positive welding outcome that the weld seam was relatively straight and almost not bent.

In the experimental group II of the synergistic effect of internal gas flow ( $Q$ ) and external gas flow ( $q$ ), there was no short-circuit transition phenomenon during the welding process according to the images of the droplet transfer (Fig. 6). When  $Q$  and  $q$  work together, the overall gas flow rate increased, resulting in an increase in the gas flow velocity  $v_f$ . As  $v_f$  increased, the plasma flow force  $F_d$  also increased sharply according to formula (4), which further promotes the droplet transition process and suppresses the occurrence of short-circuit transition. Under the premise of  $q=40\text{L/min}$ , the droplet transition period generally showed a decreasing trend with the increase of  $Q$ , but the transferring period slightly increased overall compared to the control group, and the overall droplet transition period was slightly reduced compared to experimental group I. At the same time, there was almost no change in droplet size; however, the overall droplet size slightly increased compared to the control group, while the overall droplet size slightly decreased compared to experimental group I. There were similarities between experimental group II and I in surface morphology of the weld seam, with a relatively uniform and straight weld seam formation. And the surface morphology of the weld seam was better than that of the control group since there was no short-circuit transition and no weld nodules. This further demonstrated that the addition of external gas flow could improve the state of force imbalance during the droplet falling process, making the weld seam straight.

## 4.2 Cross section of weld seam

### 4.2.1 Pores

Several visible pores could be clearly observed by inspecting Figs. 13, 15, and 17. This study utilized Fluent software to numerically simulate the synergistic effect of internal and external Ar gas flow to assist in explaining the reasons for the formation of these pores.

We simplified the structure of the MIG welding torch and established an equivalent two-dimensional model as shown in Fig. 21a. The mesh partitioning results of this model are shown in Fig. 21b, with a mesh size of 0.3 mm. The volume of fluid (VOF) model was utilized for numerical simulation of two-phase gas flow. Before the simulation, it was necessary to simplify the arc plasma as a high-temperature and high flow rate argon ion flow, without taking the influence

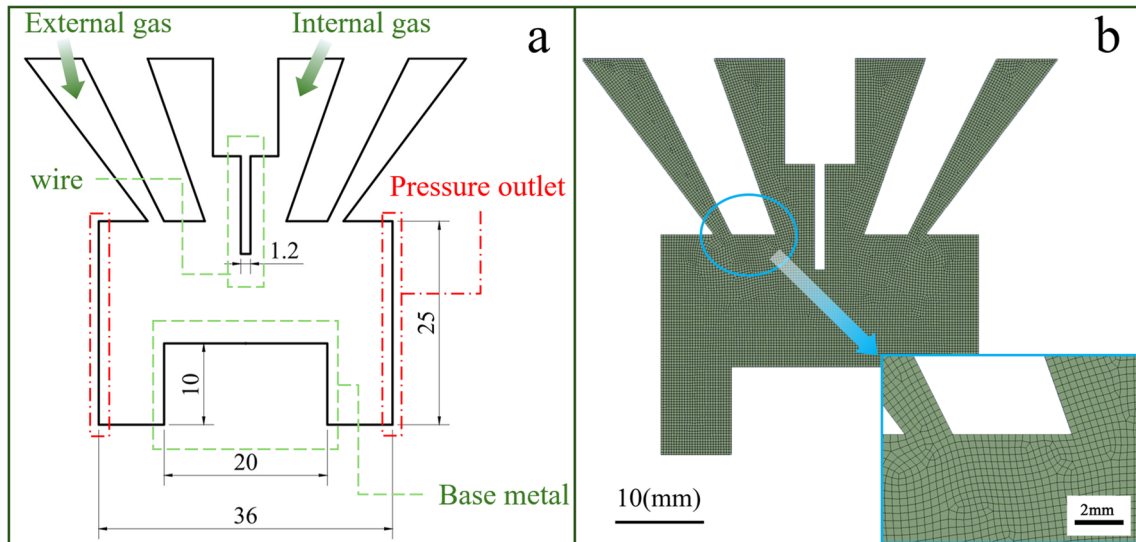


**Fig. 21** Simplified numerical simulation model diagram: **a** equivalent two-dimensional model; **b** grid partitioning diagram

of electromagnetic force on it into consideration, to improve computational efficiency.

During the calculation process, the temperature of the arc argon ion flow was set to 8000 K, the flow rate was set to 80 m/s [35]. Both internal and external gas flow inlets were velocity inlets, with the inlet velocity converted based on the corresponding flow rate, and all outlets were pressure outlets. Since this experiment primarily focused on the impact of composite internal and external gas flow on titanium alloy MIG welding, and the shielding gas within the tail cover remained a uniform, stable, and low-velocity laminar flow, its effect on the molten pool could be negligible during welding. Consequently, the tail cover was not taken into account in the simulation. During the simulation process, the control equations followed between argon, air, and boundary substances included the mass-conservation equation, momentum-conservation equation and energy-conservation equation, as shown in Eqs. (6) to (8)[36].

The mass-conservation equation is:

$$\frac{\partial \rho}{\partial t} + \frac{\partial(\rho u)}{\partial x} + \frac{\partial(\rho v)}{\partial y} = 0 \tag{6}$$

where  $\rho$  is density of the fluid,  $t$  is time, and  $u$  and  $v$  are the velocity component.

The momentum-conservation equation is:

$$\begin{cases} \frac{\partial(\rho u)}{\partial t} + \text{div}(\rho uu) = -\frac{\partial P}{\partial x} + \frac{\partial \tau_{xx}}{\partial x} + \frac{\partial \tau_{yx}}{\partial y} + F_x \\ \frac{\partial(\rho v)}{\partial t} + \text{div}(\rho vu) = -\frac{\partial P}{\partial y} + \frac{\partial \tau_{xy}}{\partial x} + \frac{\partial \tau_{yy}}{\partial y} + F_y \end{cases} \tag{7}$$

where  $\rho$  is the pressure on flowing microelements,  $\tau_{ij}$  is the components of viscous force  $\tau$  in all directions ( $i, j = x, y$ ), and  $F_x$  and  $F_y$  are the volume forces on the fluid element.

The energy-conservation equation is:

$$\frac{\partial(\rho T)}{\partial t} + \text{div}(\rho u T) = \left( \frac{k}{c_p} \text{grad} T \right) + S_T \tag{8}$$

where  $T$  is the fluid temperature,  $c_p$  is the specific heat capacity,  $k$  is the fluid thermal propagation coefficient, and  $S_T$  is the viscous dissipation term.

In the numerical simulation process, the air and argon were taken into consideration as main gases, and their physical parameters are shown in Table 3.

Reynolds number was usually used to determine the laminar and turbulent state of the fluid when selecting the physical model of fluid flow state in the computational domain. Reynolds number  $R_e$  is shown in formula (9).

$$R_e = \frac{\rho u L}{\mu} \tag{9}$$

where  $\rho$  is the fluid density,  $u$  is the flow velocity,  $L$  is the feature length, and  $\mu$  is the dynamic viscosity.

**Table 3** Gas physical parameters

Type	Density (kg/m <sup>3</sup> )	Viscosity (× 10 <sup>-5</sup> Pa·s)	Thermal conductivity coefficient [W/(m·K)]	Specific heat capacity [kJ/(kg·°C)]
Air	1.225	1.7894	0.0244	1.00643
Argon	1.782	2.0900	0.0173	0.51916

The corresponding Reynolds number was calculated based on the internal flow rate  $Q$  and the external flow rate  $q$ , as shown in Table 4. Generally, when  $R_e$  was less than 2000, the fluid flow state was considered laminar, while  $R_e > 4000$ , the fluid flow state was considered turbulent, and it was the region of transition from laminar to turbulent flow when  $2000 < R_e < 4000$ . It was evident that the calculation results of  $R_e$  in Table 4 demonstrated that a portion of Reynolds numbers for the flow velocity were in laminar flow, whilst another was in the transition region, indicating that not all flow states in the computational domain belonged to laminar flow. Therefore, the k- $\omega$  SST turbulence model was utilized for this numerical simulation.

The schematic diagram of the welding process under the independent action of the internal gas flow is shown in Fig. 22a. It was evident that the cover range provided by shielding gas  $Q$  was limited based on the numerical simulation results (Fig. 22b), forming a poor shielding coverage. Therefore, air was easily mixed into the molten pool during the welding process, resulting in porosity defects in the weld seam.

The schematic diagram of the welding process under the separate action of external gas flow is shown in Fig. 23a.

**Table 4** Reynolds number corresponding to different gas flow rates

	Argon gas flow /(L/min)	Argon gas flow rate (m/s)	$R_e$
$Q$	10	0.415	1061.524
	15	0.622	1591.008
	20	0.829	2120.491
$q$	10	0.161	411.820
	40	0.645	1649.839
	50	0.807	2064.217

When  $q$  acted alone, it was observed that a large single porosity appeared at the cross-section of the weld seam when  $q = 10\text{L}/\text{min}$ . This was because the external shielding gas at this time failed to cover the molten pool, causing a large amount of air to enter the molten pool and form porosity followed, based on the numerical simulation results (Fig. 23b). However, the porosity decreased with the increase of  $q$ , and no porosity appeared at  $q = 40\text{L}/\text{min}$ . This indicated that the external shielding gas could cover the molten pool entirely at this moment. Unfortunately, as  $q$  further increased, the excessive shielding gas flow in the external path accounted for the turbulence's inhaling air and damaging the shielding; consequently, the small pores generated again in the cross-section when  $q = 50\text{L}/\text{min}$ . As shown in Fig. 23b, when  $q = 40\text{L}/\text{min}$ , while the external shielding gas could cover the molten pool, the small diameter of the gas flow enveloping the welding wire (approximately twice the wire's diameter) still failed to provide adequate protection.

The schematic diagram of the welding process under the synergistic effect of internal gas flow ( $Q$ ) and external gas flow ( $q$ ) is shown in Fig. 24a. A single small pore appeared in the cross-section of the weld seam when  $Q = 10\text{L}/\text{min}$ , which is due to the turbulent flow generated by  $Q$  and  $q$ , causing air to be drawn into the molten pool; thereby, pores followed. When  $Q = 15\text{L}/\text{min}$ , the disappearance of pores was owing to the fact that a completely coverage for the molten pool was formed by  $Q$  and  $q$  and did not generate turbulence, resulting in better shielding. But as  $Q$  increased to  $20\text{L}/\text{min}$ , small pores began to appear again, which is due to the turbulent flow occurred again drew a small amount of air into the molten pool, forming pore defects. The numerical simulation results shown in Fig. 24b were exactly consistent with this experimental phenomenon. As shown in Fig. 24b, when  $q = 40\text{L}/\text{min}$  and  $Q = 15\text{L}/\text{min}$ , the shielding gas not only effectively

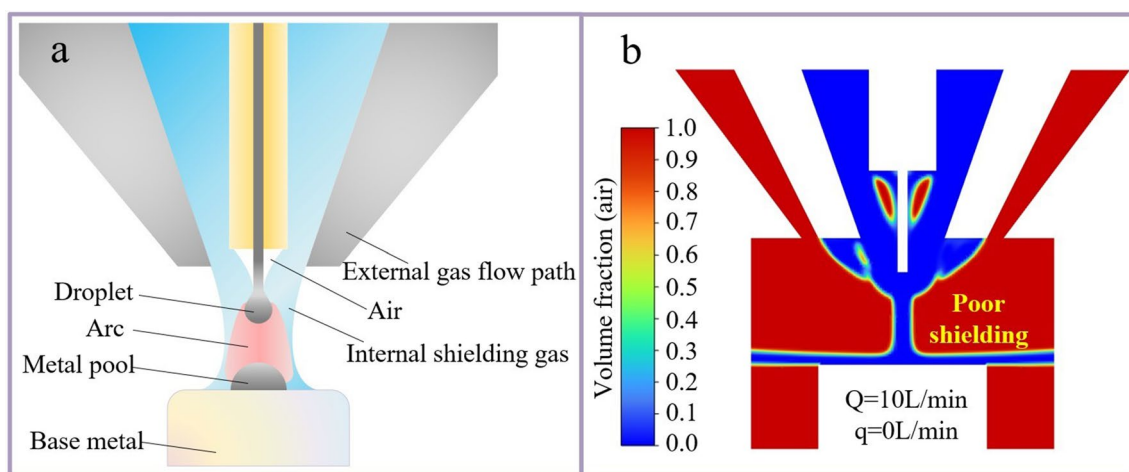


**Fig. 22** a Schematic diagram of welding process and b numerical simulation results under individual action of internal gas flow  $Q$

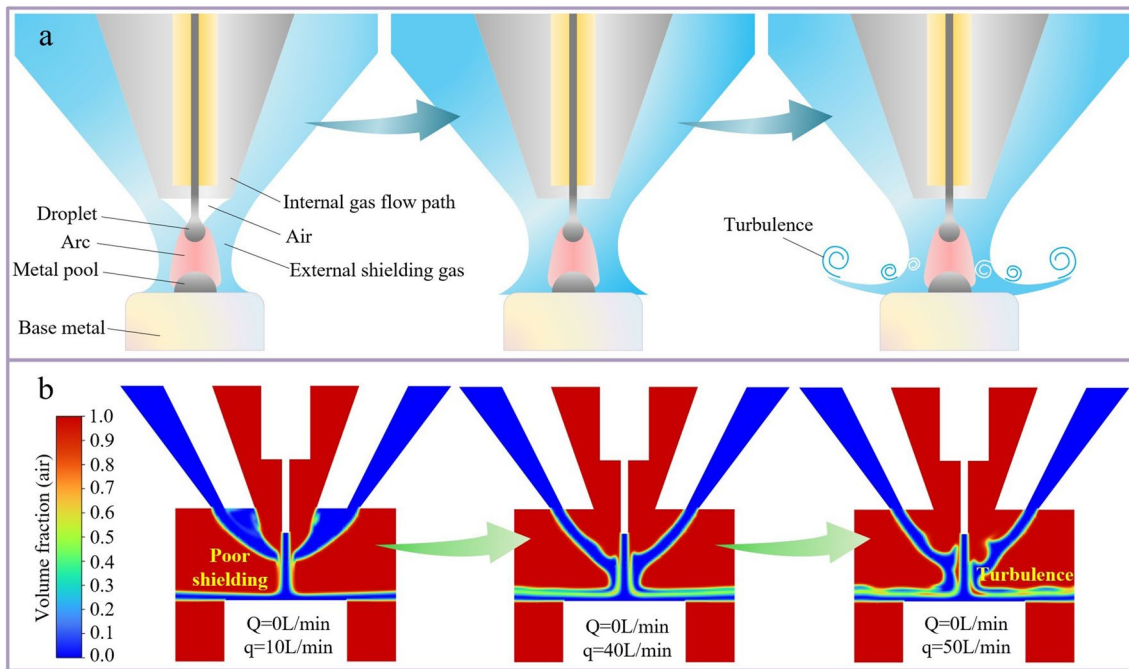


Fig. 23 a Schematic diagram of welding process and b numerical simulation results under the separate action of external gas flow  $q$

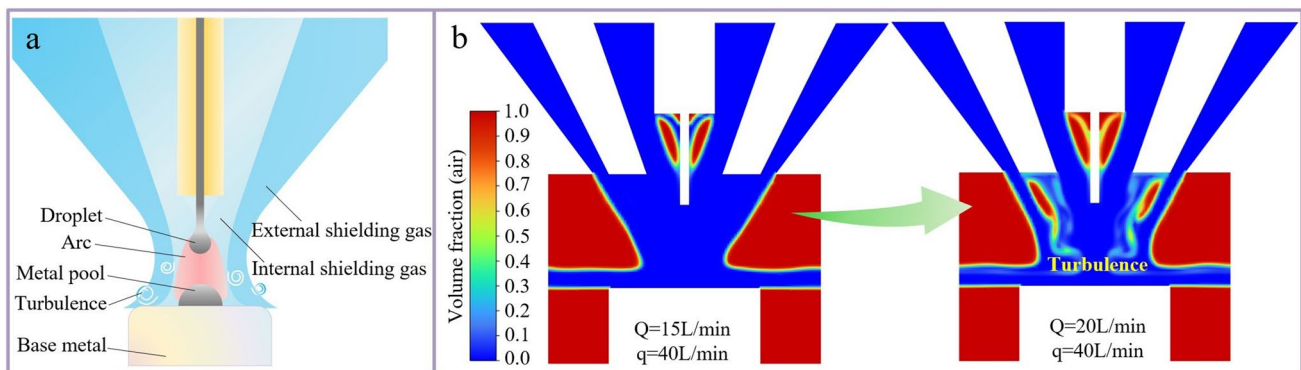


Fig. 24 a Schematic diagram of welding process and b numerical simulation results under the synergistic effect of internal gas flow  $Q$  and external gas flow  $q$

covered the molten pool but also significantly increased the diameter of the shielding gas flow around the wire (compared with Fig. 23b). Furthermore, there was no turbulence, indicating that the protective effect was optimal at this condition.

It was found that all the pores appearing in the cross-section of the weld seam were located near the edge of the molten pool through the observation in Sect. 2.3. In response to this experimental phenomenon, the following theoretical analysis was made. The speed at which pores float and escape in the welding pool can be characterized by formula (10).

$$v = K \frac{(\rho_L \rho_G) g r^2}{\eta} \tag{10}$$

where  $v$  is the escape velocity of the bubbles,  $K$  is a constant,  $\rho_L$  is the density of liquid metal,  $\rho_G$  is the gas density,  $g$  is the gravitational acceleration,  $r$  is the pores' radius, and  $\eta$  is the viscosity of liquid metal.

It could be inferred that the viscosity of liquid metal  $\eta$  had a significant impact to the speed at which bubbles float and escape according to expression (10). During the welding process, a large temperature gradient was formed in front of the solid–liquid interface [37], and the temperature near



the solid–liquid interface area (i.e., the edge of the molten pool) was lower, resulting in the viscosity  $\eta$  in this area large relatively, which reduces the upward velocity of bubbles, coupled with the fast solidification speed of the molten pool that was not conducive to the upward movement of bubbles. So, when air was drawn into the edge area of the molten pool, the viscosity and the solidification speed of the molten pool accounted for the bubbles' untimely floating upward and escaping, which are retained in the edge area of the molten pool to form pores. This explained why most of the pores found in the cross-section of the weld existed near the edge of the molten pool.

#### 4.2.2 Weld penetration and width

The greater the constraint on the arc, the more concentrated the energy of the arc when conducting a titanium alloy MIG welding. The dynamic pressure of the arc acted on the molten pool, and the depth of it became greater, making it easier to form a finger-shaped penetration. The small current, small heat input and increasing static pressure of the arc accounted for the semi-circular penetration obtained in this experiment, which is a typical geometric shape of the weld cross-section generated by “droplet” transition. Even if  $Q$  continued to increase, when the internal gas flow  $Q$  acted alone, a state of insufficient shielding still was remained for the molten pool (Fig. 22b). A slight turbulence disturbance was produced gradually by internal gas flow as it increased, which reduces the constraint effect on the arc and disperses the arc energy, followed by a continuous decrease in the penetration and an increase in the fusion width. The constraint effect on the arc was the best when  $Q = 10\text{L/min}$ , achieving the maximum depth and the minimum width of fusion. Currently, the arc during the transferring of large droplets was also the shortest, which further indicates that the compression and constraint effect of the internal gas flow on the arc was the most significant at  $Q = 10\text{L/min}$ . The arc length during the transition of small droplets decreased continuously with the increase of  $Q$ , indicating that the increase of  $Q$  had a stable compression effect on the arc. However, during the entire transition process, the transition of large droplets occupied the vast proportion of the whole time, so the compression effect of  $Q$  on the arc during the transition of small droplets could only have a small impact. Finally, the result was the experimental phenomenon dominated by the transition law of large droplets.

It was found that the arc shape was relatively chaotic by analyzing the images of the droplet transfer (Fig. 4) when the external gas flow  $q$  acted singly. This was because that both the covering range of shielding gas and the space for arc's activity were larger, which accounts for the arc's becoming longer at this moment; therefore, the arc was more significantly disturbed by  $q$ , resulting in a more unstable

arc shape. And as  $q$  increased, the arc length also changed irregularly. Both whether the arc had a concentrated energy and how much the heat input from the arc were the key factors affecting the depth and width of the fusion [38]. When the external gas flow acted alone, the overall penetration of the weld cross-section showed a decreasing trend and the fusion width changed irregularly as  $q$  increased because of almost no restraining effect applied to the arc by the external gas flow. As  $q$  increased, the arc was more disturbed with the gradually appearing turbulent phenomena (Fig. 23b), which leads to unstable arc shape and energy concentration. In addition, the external gas flow also had a certain cooling effect on the arc, which reduces the heat input of the arc to the molten pool. Therefore, it ultimately led to a decrease in the cross-sectional penetration of the weld and an irregular change in the weld width.

The arc length decreased steadily with the increase of  $Q$  when the internal gas flow  $Q$  and the external gas flow  $q$  worked together, indicating that a relatively stable compression effect of  $Q$  on the arc was approached in the atmosphere of external gas flow. According to Fig. 5, the overall arc length slightly decreased in experimental group II compared to the inner gas flow acting alone, indicating that the addition of the outer gas flow under the action of the inner gas flow was beneficial for arc compression. Analysis of Fig. 18 to Fig. 19 revealed that the weld penetration decreased as  $Q > 5\text{L/min}$ , and the weld width increased with the growth of  $Q$ . This was because that as  $Q$  increased, although the internal gas flow produced stable compression on the arc, the presence of the external gas flow not only brought the high-temperature zone closer to the base material, but also expanded the arc contact area and affected the arc temperature. Therefore, even if the arc column was compressed, the energy density decreased and the energy could not be effectively concentrated, resulting in this consequence. When  $Q = 20\text{L/min}$ , the arc length was the smallest, indicating that the internal gas flow had the greatest compression effect on the arc at present. But the weld penetration decreased sharply, and the weld width increased quickly because of the turbulence occurring for the inner and outer gas flow (Fig. 24b), causing the arc disturbed and the arc energy more dispersed. Moreover, an increase in gas flow rate cooled the arc and reduced the heat input of the arc to the melt pool. And at this point, the generated turbulence also drew air into the molten pool, resulting in porosity in the cross-section of the weld seam. Figure 19 shows that compared to  $Q$  acting alone, under the action of the inner gas flow, the addition of  $q$  reduced the depth slightly of the fusion and increased somewhat the width of it. This was because the outer gas flow caused minor disturbance to the arc, which is not conducive to the concentration of arc energy. Both the energy density of the arc and the heat input to the melt pool were decreased.



## 5 Conclusions

1. When the internal gas flow ( $Q$ ) was constant, the addition of external gas flow ( $q$ ) would increase the transition period of the droplet to a certain extent, but the rule of the transferring period did not be altered. The variation pattern of the droplet transfer was mainly influenced by  $Q$ , while the length of the period was mainly impacted by  $q$ .
2. The short-circuit transition occurred when  $q$  was not added, and the number of it increased with the growth of  $Q$ . There was no longer a short-circuit transition after adding  $q$  for the obstruction of the combined effect of  $Q$  and  $q$  on the droplet transition period and droplet size, arc length. An increase of  $Q$  would stabilize the compression of the arc in the atmosphere of  $q$  and reduce the length of the arc column; i.e.,  $q$  had a beneficial effect on the compression of the arc.
3. Both the changes in  $Q$  and  $q$  had a slightly stronger impact on the weld penetration than on the weld width. The contact area of the arc was increased and the energy density of it was reduced for the presence of  $q$ . Besides,  $q$  reduced the heat input to the molten pool with its' cooling effect to arc. Therefore, the synergistic effect would cause a certain degree of reduction in the weld penetration; however, its regulation for variation remained basically unchanged.
4. From the perspective of the forming quality, with no obvious bending and almost no weld nodules, the weld within the synergistic effect of  $Q$  and  $q$  was relatively uniform and straight. It was found that within the synergistic effect of  $Q$  and  $q$ , the arc changed stably while the variations in weld penetration and weld width were relatively regular; there was no short-circuit transition and the surface morphology of the weld was perfect, by comparing three sets of experiments. Therefore, a stable and positive forming of titanium alloy MIG welding was achieved within the synergistic effect of  $Q$  and  $q$ . When  $q=40\text{L}/\text{min}$  and  $Q=15\text{L}/\text{min}$ , the shielding gas offered extensive coverage and effective shielding without turbulence. Furthermore, the weld cross-section exhibited no pores, establishing it as the optimal gas flow configuration in the experiment.

**Author contribution** All authors contributed to the study conception and design. Material preparation, data collection, and analysis were performed by Chuanchuan Jia, Guorui Sun, Boqiao Ren, Jiuqing Liu, and Chao Chen. The first draft of the manuscript was written by Chuanchuan Jia and all authors commented on previous versions of the manuscript. All authors read and approved the final manuscript.

**Funding** The authors were grateful for the generous support from the National Natural Science Foundation of China (No. 52305362).

**Declarations** The manuscript was approved by all authors for publication.

**Conflict of interest** The authors declare no competing interests.

## References

1. Sen R, Choudhury SP, Kumar R et al (2018) A comprehensive review on the feasibility study of metal inert gas welding[J]. *Mater Today : Proc* 5(9):17792–17801
2. Sunny KT, Korra NN (2021) A systematic review about welding of super austenitic stainless steel[J]. *Mater Today: Proc* 47:4378–4381
3. Karayel E, Bozkurt Y (2020) Additive manufacturing method and different welding applications[J]. *J Market Res* 9(5):11424–11438
4. Wang B, Hu SJ, Sun L et al (2020) Intelligent welding system technologies: state-of-the-art review and perspectives[J]. *J Manuf Syst* 56:373–391
5. Sai MS, Dhinakaran V, Kumar KPM et al (2020) A systematic review of effect of different welding process on mechanical properties of grade 5 titanium alloy[J]. *Mater Today: Proc* 21:948–953
6. Dhinakaran V, Varsha Shree M, Jagadeesha T et al (2020) A review on the recent developments in modeling heat and material transfer characteristics during welding[J]. *Mater Today: Proc* 21:908–911
7. Gao Z, Li Y, Shi H et al (2023) Microstructure characteristics under varying solidification parameters in different zones during CMT arc additive manufacturing process of 2319 aluminum alloy[J]. *Vacuum* 214:112177
8. Haque SR (2023) Investigation on welding defects of alloys using TIG and MIG welding[J]. *Hybrid Advances* 3:100066
9. Jia H, Cao L, Fu S et al (2023) Numerical simulation and experiment for the dynamic behavior of molten pool in ultrasonic-assisted MIG welding[J]. *Int J Heat Mass Transf* 215:124469
10. Wu X, Liu T, Cai W (2015) Microstructure, welding mechanism, and failure of Al/Cu ultrasonic welds[J]. *J Manuf Process* 20:321–331
11. Kumar S, Wu CS, Padhy GK et al (2017) Application of ultrasonic vibrations in welding and metal processing: a status review[J]. *J Manuf Process* 26:295–322
12. Pavan AR, Arivazhagan B, Vasudevan M et al (2023) Study on the microstructure and mechanical properties of hybrid laser + MIG welded joints of 316LN stainless steel[J]. *Opt Laser Technol* 163:109410
13. Shen L, Chen H, Che X et al (2020) Stress corrosion cracking behavior of laser-MIG hybrid welded 7B05-T5 aluminum alloy[J]. *Corros Sci* 165:108417
14. Liu F, Xu B, Song K et al (2022) Improvement of penetration ability of heat source for 316 stainless steel welds produced by alternating magnetic field assisted laser-MIG hybrid welding[J]. *J Mater Process Technol* 299:117329
15. Yuji T, Tashiro S, Kinoshita H et al (2024) An investigation on plasma-MIG hybrid welding process of thick plate aluminum[J]. *J Adv Join Process* 9:100188
16. Huang A, Zhang J, Gao C et al (2019) Effects of groove constraint space on plasma characteristics during Laser-MIG hybrid welding of Titanium alloy[J]. *J Manuf Process* 48:137–144
17. Balasubramanian M, Jayabalan V, Balasubramanian V (2008) A mathematical model to predict impact toughness of pulsed-current

- gas tungsten arc-welded titanium alloy[J]. *Int J Adv Manuf Technol* 35(9–10):852–858
18. de Oliveira Campos F, Araujo AC, Jardini Munhoz AL et al (2020) The influence of additive manufacturing on the micromilling machinability of Ti6Al4V: a comparison of SLM and commercial workpieces[J]. *J Manuf Process* 60:299–307
  19. Kumar C, Das M, Paul CP et al (2017) Experimental investigation and metallographic characterization of fiber laser beam welding of Ti-6Al-4V alloy using response surface method[J]. *Opt Lasers Eng* 95:52–68
  20. Eickhoff ST (1990) Characterization of spatter in low-current GMAW of titanium alloy plate[J]. *Weld J* 69(10):382
  21. Cao W, Guo Y, Zhang H et al (2021) Application of container technology in numerical ocean model: a kind of high-performance ROMS containerized architecture[J]. *J Phys: Conf Ser* 1961(1):12046
  22. Xu X, Song G, Zhao S et al (2020) Effect of distance between the heat sources on energy transfer behavior in keyhole during laser-GTA welding titanium alloy[J]. *J Manuf Process* 55:317–325
  23. Zhang YM, Li PJ (2001) Modified active control of metal transfer and pulsed GMAW of titanium[J]. *Weld J* 80(2):54–61
  24. Yu J, Cai C, Xie J et al (2023) Weld formation, arc behavior, and droplet transfer in narrow-gap laser-arc hybrid welding of titanium alloy[J]. *J Manuf Process* 91:44–52
  25. Denney PE, Shinn BW, Fallara PM (2005) Laser plus GMAW hybrid welding of titanium[J]. Edison Welding Institute Columbus Ohio USA
  26. Shinn BW, Farson DF, Denney PE (2005) Laser stabilisation of arc cathode spots in titanium welding[J]. *Sci Technol Weld Join* 10(4):475–481
  27. Li G, Wang Y, Liang Y et al (2024) Microstructure and mechanical properties of laser welded Ti-6Al-4V (TC4) titanium alloy joints[J]. *Opt Laser Technol* 170:110320
  28. de Meneses VA, Gomes JFP, Scotti A (2014) The effect of metal transfer stability (spattering) on fume generation, morphology and composition in short-circuit MAG welding[J]. *J Mater Process Technol* 214(7):1388–1397
  29. Chen Y, Yang Z, Xu K et al (2023) Effect of energy parameters on droplet transfer behavior and weld formation in laser-arc hybrid welding with cable-type welding wire[J]. *J Market Res* 26:4191–4205
  30. Liu F, Yang B, Sun H et al (2023) Mechanism investigation for the influence of laser power on droplet transfer behaviors in laser-MIG hybrid welding[J]. *Opt Laser Technol* 157:108750
  31. Uddin E, Iqbal U, Arif N, et al (2019) Analysis of metal transfer in gas metal arc welding[J]. *AIP Conf Proc* 2116(1)
  32. Zhao Y, Chung H (2018) Numerical simulation of the transition of metal transfer from globular to spray mode in gas metal arc welding using phase field method[J]. *J Mater Process Technol* 251:251–261
  33. Liu S, Liu F, Zhang H et al (2012) Analysis of droplet transfer mode and forming process of weld bead in CO<sub>2</sub> laser-MAG hybrid welding process[J]. *Opt Laser Technol* 44(4):1019–1025
  34. Choi JH, Lee J, Yoo CD (2001) Dynamic force balance model for metal transfer analysis in arc welding[J]. *J Phys D: Appl Phys* 34(17):2658–2664
  35. Hu J, Tsai HL (2007) Heat and mass transfer in gas metal arc welding. Part I: The arc[J]. *Int J Heat Mass Transf* 50(5):833–846
  36. Huang W, Zhang Y (2019) Finite element simulation of thermal behavior in single-track multiple-layers thin wall without-support during selective laser melting[J]. *J Manuf Process* 42:139–148
  37. Liu H, Fang M, Han Y et al (2023) Achieving strength-ductility combination and anisotropy elimination in additively manufactured TiB/Ti6Al4V by in-situ synthesized network architecture with fine grains[J]. *Compos B Eng* 262:110822
  38. Zorin IV, Artem EVAA, Lysak VI et al (2023) Structure formation and properties of nickel aluminide-based alloy deposited by the GMAW method under periodic arc thermal impact on the weld pool[J]. *J Mater Proc Technol* 319:118085

**Publisher's Note** Springer Nature remains neutral with regard to jurisdictional claims in published maps and institutional affiliations.

Springer Nature or its licensor (e.g. a society or other partner) holds exclusive rights to this article under a publishing agreement with the author(s) or other rightsholder(s); author self-archiving of the accepted manuscript version of this article is solely governed by the terms of such publishing agreement and applicable law.